Topochemical transformation of two-dimensional single crystalline $Na_{0.5}Bi_{0.5}TiO_3$-$BaTiO_3$ platelets from $Na_{0.5}Bi_{4.5}Ti_4O_{15}$ precursors and their piezoelectricity

Chao Jiang,[1,3] Dou Zhang,[1*] Kechao Zhou,[1] Haixue Yan,[2] Hangfeng Zhang,[3] and Isaac Abrahams[3*]

[1]State Key Laboratory of Powder Metallurgy, Central South University, Changsha 410083, China.

[2]School of Engineering and Materials Sciences, Queen Mary University of London, Mile End Road, London, E1 4NS, UK.

[3]School of Biological and Chemical Sciences, Queen Mary University of London, Mile End Road, London, E1 4NS, UK

*Corresponding Authors

Dou Zhang, Email: dzhang@csu.edu.cn

Isaac Abrahams, Email: i.abrahams@qmul.ac.uk

Abstract

Two-dimensional monocrystalline platelets of the perovskite structured lead–free system $(Na_{0.5}Bi_{0.5})_{0.93}Ba_{0.07}TiO_3$ (NBBT) were synthesized from platelets of layer-structured $Na_{0.5}Bi_{4.5}Ti_4O_{15}$ (NBIT), using a topochemical route. Both NBIT and NBBT platelets showed high aspect ratios with an average size of 10 μm and thickness of 0.6 μm, for the latter. A structural transformation from layer-structured NBIT to perovskite NBBT was identified in a transitional platelet, which contained phases of both NBIT and NBBT. The composition of NBBT lies at a morphotropic phase boundary (MPB), with the coexistence of monoclinic and tetragonal polymorphs confirmed by X-ray powder diffraction analysis. Transmission electron microscopy and piezoresponse force microscopy were used to investigate the domain structure, with stripe-like domains in the unpoled system transformed into lamellar domains after poling. The piezoresponse amplitude for a NBBT platelet indicated a large piezoresponse strain, corresponding to a field-induced strain S_{max}/E_{max} of around 800 pm/V at 5 kV/mm, which is significantly higher than that in ceramic samples of NBBT at the same applied potential.

1. Introduction

Energy harvesting (EH) [1-3] and nanoelectromechanical (NEM) systems [4-7] have attracted great interest in the scientific and engineering communities, due to their potential application in smart and portable electronic devices. Flexible and stretchable nanogenerators, which are capable of exhibiting strain induced piezoelectric polarization, are typically the core part of EH systems for scavenging small amounts of energy effectively, through mechanical action such as rolling, bending, or even applied pressure through human motion. [8-10] NEM systems are often integrated with micro/nano- mechanical resonators, which can oscillate and create electrical signals at very high resonant frequencies, due to their small size and remarkable sensing and detection ability. [6,7]

Recently, several piezoelectric materials with a variety of micro/nano-structures and device configurations have been successfully developed. Initial work focused on ZnO based systems. [11-18] However, the piezoelectric response of ZnO is limited and so attention switched to other materials, such as $PbZr_xTi_{1-x}O_3$ (PZT), [19-21] which exhibits excellent piezoelectric behaviour. However, there are important environmental concerns regarding the use of PZT based materials, due to the toxicity of lead and current work is focused on lead free alternatives. Several lead-free materials show the potential to replace lead based systems. The solid solution system $(Na_{0.5}Bi_{0.5})_{1-x}Ba_xTiO_3$ (NBBT) [22-30] has received considerable attention in recent years due to its high piezoelectric coefficient near the morphotropic phase boundary (MPB) in the compositional range $0.05 \leq x \leq 0.07$.

NBBT materials at the MPB have been intensively studied. Maurya *et al.* [23] prepared textured NBBT ceramics with piezoelectric response values as high as 300 pC/N. Levin and Reaney, [31] Ma *et al.* [32,33] and Dittmer *et al.* [34] used transmission electron microscopy (TEM) and piezoresponse force microscopy (PFM) techniques to study the microstructure of NBBT ceramics and their domain transformation processes under electric fields. Their studies proved NBBT materials at the MPB had large piezoelectric responses and explained the origins of these. Despite extensive studies on NBBT ceramics, the influence of different micro/nano-structures has seldom been reported. Maurya *et al.* [35] reported the synthesis and characterization of NBBT whiskers, which were used as templates to prepare textured ceramics. Compared to the one-dimensional morphology of whiskers, the two-dimensional morphology of monocrystalline platelets could be advantageous for particular applications. We have shown that incorporation of NBBT platelets into polymer composites leads to materials with excellent energy storage properties. [36] Potential applications for the platelets include using them as substrates for the growth of nanowire arrays to assemble nanogenerators and nanosensors [37-39] and using micro/nano fabrication techniques, such as focused ion beam lithography, on platelets to prepare EH microdevices and high frequency NEM systems. [40,41]

The synthesis of two-dimensional NBBT platelets is challenging due to their perovskite structure, which typically results in the growth of cubic crystals. In the present work, a topochemical route is developed for the synthesis of NBBT platelets, TEM and PFM are used to investigate the piezoelectric properties of these platelets

and understand their origins, in particular, changes in ferroelectric domain structure as a result of poling.

2. Experimental

2.1 Synthesis of single crystalline NBBT platelets

Bi_2O_3 (99.9%), TiO_2 (99.9%), Na_2CO_3 (99.9%), $BaCO_3$ (99.9%) and NaCl (99.5%), obtained from Sinopharm Chemical Reagent Co. Ltd. China, were used as starting materials. NBBT was synthesized in a two-step process. Initially, NBIT was prepared from stoichiometric amounts of Bi_2O_3, TiO_2 and Na_2CO_3 using a molten salt synthesis method. The starting materials were mixed with an equal weight of NaCl and ball milled for 24 h in ethanol. The mixture was then dried at 60 °C. The dried mixture was heated at 1050 °C for 4 h in a covered alumina crucible, before cooling in the furnace to room temperature. The resulting NBIT platelets were separated by washing with hot deionized water to remove the NaCl (using $AgNO_3$ solution to confirm complete removal of NaCl).

The NBIT platelets were used as precursors in the synthesis of NBBT platelets of composition $(Na_{0.5}Bi_{0.5})_{0.93}Ba_{0.07}TiO_3$. To preserve the platelet morphology of the NBIT crystals, stoichiometric amounts of NBIT, Na_2CO_3, $BaCO_3$ and TiO_2 were mixed with an equal weight of NaCl as a suspension in ethanol, with a magnetic stirrer at 60 °C and the ethanol evaporated. The dried mixture was placed in a covered alumina crucible at 950 °C for 6 h, before cooling to room temperature in the furnace. The product was washed with hot deionized water several times to remove the salt

(using $AgNO_3$ solution to confirm this) and dried at 80 °C for 24 h.

2.2 Fabrication of TEM and PFM samples

For TEM, the NBBT platelets were first mechanically crushed in liquid nitrogen, while for PFM measurements, the platelets were dispersed in ethanol and dropped onto a thin Pt coated Si conductive wafer, with a thickness of 1 mm. After drying at 60 °C for 8 h, the wafer was treated at 500 °C for 10 h.

2.3 Poling

Poling was conducted on platelet samples at 80 °C, using a potential of 8 kV and a point source height of 70 mm, with a corona poling system (HYJH-Y10/3, Xianyang Huiyuan Automation Equipment Co. Ltd.).

2.4 Characterization

Phase identification was carried out using X-ray powder diffraction (XRD) analysis, with graphite monochromated Cu-Kα radiation (λ = 1.5418 Å, D500, Siemens Inc., USA), over the 2θ range 5 to 100°, in steps of 0.001°, with a count time of 4 s per step. Structure refinement was carried out using the Rietveld method with the GSAS suite of programs [42] Starting models were based on the structures reported by Blanchard *et al*. [43] and Jones and Thomas, [44] for the monoclinic (*Cc*) and tetragonal (*P*4*bm*) polymorphs of $Na_{0.5}Bi_{0.5}TiO_3$, respectively, with appropriate substitution of Na/Bi by Ba. Atomic parameters were not refined in the analysis. The morphologies were

observed by scanning electron microscopy (SEM, model JMS 6460LV, JEOL, Tokyo, Japan). TEM (JEOL, JEM-2100 F, Japan) was used to study the NBIT to NBBT structural transformation process, with an accelerating voltage of 200 kV.

A commercial scanning probe microscope (Nanoscope V, Bruker Instruments Inc.) was used for PFM measurements. A Pt/Ir coated conductive tip (SCM-PIT, Bruker Instruments Inc.), with a resonant frequency of 75 kHz, a spring constant of 2.8 N m, and length 125 μm was utilized in this study. The PFM images represent the "piezoresponse" signal measured by AFM equipped with a lock-in. Only the out-of-plane vibration direction perpendicular to the sample surface of the tip was recorded.

3. Results and Discussion

3.1 Topochemical transformation of NBBT platelets

The XRD patterns of the NBIT and NBBT platelets were both in good agreement with the corresponding JCPDS standard patterns (nos. 74-1316 and 89-3109, respectively). Close inspection of the XRD pattern for the NBBT platelets (Fig. 1) shows splitting of peaks indicative of the coexistence of at least two polymorphs of NBBT and is consistent with the composition being close to the MPB. A number of different polymorph combinations were used to try to model the data, with a mixture of the tetragonal (*P*4*bm*) and monoclinic (*Cc*) polymorphs resulting in a significantly better fit to the observed data (Fig. 2 (a)) than other models. The monoclinic phase is very closely related to the rhombohedral (*R*3*c*) phase. Indeed, in pure $Bi_{0.5}Na_{0.5}TiO_3$ the *R*3*c* phase, characterized by $a^- a^- a^-$ octahedral tilting along the pseudo-cubic [111]

axis, had long been reported as the stable phase at room temperature, until recently when its average structure was shown to be monoclinic with $a^- a^- c^-$ octahedral tilting [31]. Barium substitution into $Bi_{0.5}Na_{0.5}TiO_3$ has been shown to induce a transition from the *Cc* phase to the true rhombohedral *R*3*c* phase at around 3-4 mol% substitution, [32] followed by a transition to the tetragonal *P*4*bm* phase at around 6%. In the present work, the apparent coexistence of the monoclinic and tetragonal phases at a composition close to the MPB might be attributable to the novel synthesis method, which may afford the isolation of a non-equilibrium state. The unit cell volume of the monoclinic phase in the present study is significantly larger than that of the unsubstituted $Bi_{0.5}Na_{0.5}TiO_3$ (235.35 $Å^3$)[43] consistent with the the substitution of the smaller Bi^{3+}/Na^+ cations with larger Ba^{2+} cations (r = 1.17, 1.18 and 1.42 Å, respectively for the ions in 8-coordinate geometry).[45]

Fig. 3 (a) and (b) show the morphology of NBIT platelets, which have dimensions in the range 5 to15 μm, with thicknesses of 0.5 to 0.8 μm. The high aspect ratios and regular shape of the NBIT platelets are retained in the topochemical reaction to make NBBT. Fig. 3 (c) and (d) show SEM images of the NBBT platelets. Most of the NBBT crystals preserved the plate-like morphology of the NBIT precursor, with an average size of 10 μm and a thickness of 0.6 μm. Such two-dimensional platelets with high aspect ratios are particularly suitable for preparing textured ceramics [23,26] and assembling NEM systems.[41] Fig. 4 shows SEM EDX mapping images of a single NBBT platelet, which confirm a uniform distribution of the constituent elements Na, Bi, Ba, Ti and O.

Fig. 5 shows high resolution TEM images of platelets before (Fig. 5 (a)) and after (Fig. 5 (c)) the topochemical reaction, with Fig. 5 (b) showing a partially reacted platelet. A lattice image of an NBIT crystal is illustrated in Fig. 5 (a) which shows a typical layer type structure. Two dimensional lattice fringes are clearly seen in this image, with interplanar spacings of 2.9 and 6.7 Å, corresponding to the (109) and (006) planes, respectively. Although XRD results indicated the complete transformation from NBIT precursors to NBBT platelets, some remaining NBIT phase was found within a NBBT platelet in TEM images, as shown in Fig. 5 (b). The transitional area where the lattice changes from NBIT to NBBT is indicated in the image. The image also gives valuable information about the mechanism of this structural transformation. Fig. 5 (c) shows the high resolution TEM image of a NBBT platelet. The measured *d*-spacings were 2.8 and 3.9 Å, which could correspond to the (101) and (001) planes of the pseudo-cubic perovskite subcell, respectively. The *d*-spacings of the (101) and (001) planes are slightly larger than those of pure NBT, and are consistent with the increase in unit cell volume seen in the XRD analysis, attributed to the chemical expansion of the lattice. Fast-Fourier transforms (FFT) of selected areas from the lattice images of NBIT and NBBT were indexed on the [010] zone axis (Fig. 5(a) and 5(c) inset) and confirmed both the selected NBIT and NBBT platelets were monocrystalline.

NBIT has an Aurivillius layer-type structure consisting of perovskite like blocks interleaved with layers of $(Bi_2O_2)_n^{2n+}$ which can be represented by a formula $(Bi_2O_2)_n^{2n+}(Na_{0.5}Bi_{2.5}Ti_4O_{15})_n^{2n-}$ where Bi^{3+} and Na^{+} correspond to the perovskite

A-site with twelvefold coordination, and Ti^{4+} is the perovskite B-site cation in six-fold coordination. [46] The bismuthate and perovskite blocks are highlighted in the high resolution TEM image in Fig. 6 (a). Fig. 6 (b) illustrates the structural transformation from NBIT to NBBT. During the topochemical reaction, the bismuthate layers are effectively replaced by perovskite layers, with Bi^{3+} ions throughout the structure partially replaced by Na^{+} and Ba^{2+}. In doing so, NBIT transforms into NBBT without extensive rearrangement of the structural framework.

3.2 Polarization behaviour

Both the tetragonal and monoclinic polymorphs are still evident after poling (Fig. 2(b)), although there are significant differences in the relative intensities of the peaks associated with the individual phases (Fig.1). Table 1 summarizes the structural and refinement parameters resulting from Rietveld analysis of the X-ray diffraction data of NBBT platelets, before and after poling. It is evident from the results presented in Table 1 that poling has the effect of increasing the monoclinic fraction of the platelets, to give roughly equal weight fractions of both polymorphs. Additionally, there is a 1% increase in unit cell volume for both polymorphs as a result of poling. It is known that poling at high fields in ceramics of compositions near the MPB in this system favours the transition to the rhombohedral phase from both the tetragonal [47] and monoclinic [32] polymorphs. Both of these transitions are achieved by changes in the octahedral tilting and are accompanied by increases in macroscopic strain. In the present study, where poling was carried out on powder samples using the corona method, the extent of induced polarization in the samples is expected to be significantly lower than in

ceramic samples. Thus, only a small lowering of the tetragonal weight fraction is observed, while there is no evidence in the X-ray data of the *Cc* to *R*3*c* transition. However, the small increase in lattice parameters observed in both monoclinic and tetragonal polymorphs after poling points to increased structural disorder in the average structure, which would be a precursor to the transition to the rhombohedral phase.

Fig. 7 shows TEM images along the [001] zone axis of a platelet of NBBT. The bright field image of the unpoled sample in Fig. 7 (a) displays clear brightness contrasts, which indicate the presence of strip-like domains, due to uneven charge distribution. These domains can be envisaged as ordered regions in a disordered matrix. The brightness contrast image shows parallel strips with approximately 90° and 180° domain boundaries, indicated in Fig 7 (a). These types of features are typical of the domain configurations of NBBT and are considered to arise from the release of internal stress by the 90° domain boundaries. [48-50] The selected area diffraction pattern of the unpoled sample in Fig. 7 (b) confirms the selected platelet has tetragonal symmetry, showing superlattice ordering of the perovskite subcell, with reflections of the type ½ (ooe) (o and e denote odd and even Miller indices, respectively), as marked by rings in the image. [33] After poling at 8 kV/mm, the strip-like domains coalesce, as shown in Fig. 7 (c). The corresponding selected-area electron diffraction pattern (Fig. 7 (d)), shows significant differences to that of the unpoled sample, including changes in relative intensity and the disappearance of ½ (ooe) superlattice reflections along the pseudo-cubic [001] zone, consistent with a change to *Cc* symmetry.

To further understand the ferroelectric behaviour and domain structure of single-crystalline NBBT platelets, PFM was employed. Figs. 8 (a)-(c) show the out-of-plane piezoresponse images for an unpoled NBBT platelet. These results clearly show the domain structure of the platelets. The unpoled platelet exhibited small size domains and irregular domain walls, consistent with the bright field TEM image shown in Fig. 7. In order to study the effects of poling on the domain structure through piezoresponse, the samples were poled at 8 kV/mm. Subsequently, the sample was scanned with a small a.c. voltage (1 V, peak-to-peak) for imaging. The corresponding images of the sample after poling are shown in Figs. 8 (d)-(f). After poling, the domains in the NBBT platelet became more ordered and homogeneous, and changed from an irregular strip-like shape to a lamellar shape. The PFM phase images reveal interesting details of the poling and domain switching processes in NBBT. Poling with an electric field applied upwardly perpendicular to the platelet surface leads to the formation of more uniform polarized domains. It is believed that the evolution of crystal structure and domain morphology during the poling-induced phase transitions in NBBT inevitably leads to large piezoelectric strain.[47]

The phase-voltage curve, measured at a scanning rate of 1 Hz is shown in Fig. 9 (a) and shows hysteresis typical of ferroelectric behaviour. The strain response of the NBBT platelets was calculated according to the coefficient of the platelet thickness and the deflection (Fig. 9 (b)). The monocrystalline NBBT platelet exhibited excellent actuating performance, with up to 0.4 % free strain at 5 kV/mm at room temperature. The value of field-induced strain S_{max}/E_{max} was calculated to reach around 800 pm/V

at 5 kV/mm. This compares to a value in textured ceramic samples of the same composition of around 500 pm/V at 5 kV/mm.[26] The high piezoelectric response is related to the electric field induced phase transition and domain switching, consistent with the work of Zhang *et al*.[28] who suggested that the exceptionally high strain of tetragonal $0.91Bi_{0.5}Na_{0.5}TiO_3$-$0.06BaTiO_3$-$0.03AgNbO_3$ crystals is mostly due to electric field induced domain switching and transition from ergodic relaxor to ferroelectric behaviour. The higher piezoelectric response of crystalline NBBT platelets compared to ceramics of the same composition make them attractive for application in flexible and stretchable piezoelectric devices, such as EH and NEM systems, where a high output electrical signal is required.

4. Conclusions

NBBT platelets were synthesized using NBIT platelets as precursors by a topochemical reaction method. The high aspect ratio of the NBIT precursor is maintained in the NBBT product. During the topochemical reaction, the bismuthate layers are effectively replaced by perovskite layers, with Bi^{3+} ions throughout the structure partially replaced by Na^+ and Ba^{2+}. In contrast to previous studies on ceramic samples, the monoclinic and tetragonal polymorphs are found to coexist in $(Na_{0.5}Bi_{0.5})_{0.93}Ba_{0.07}TiO_3$, which may be a result of the novel processing route. For NBBT platelets, two types of domain configurations including 90° and 180° arrangements are observed, as well as the electric field induced domain evolution, where strip-like domains coalesce into thin lamellar domains. The final NBBT

platelets had large piezoelectric responses, with up to 0.4 % free strain at 5 kV/mm at room temperature and a field-induced strain S_{max}/E_{max}, significantly higher than in isocompositional ceramics at the same applied potential.

Acknowledgments

This work was financially supported by the Defence Industrial Technology Development Program, China (grant no. A1420133028) the Natural Science Foundation of China (grant no: 51072235), Hunan Nonferrous Research Funding (grant no: YSZN2013CL05), Hunan Doctoral Research Innovation Project (grant no: CX2014B055) and China Scholarship Council (grant no: 201506370175).

References

1 Z. L. Wang, J. Chen and L. Lin, *Energ. Environ. Sci.*, 2015, 8, 2250-2282.

2 Z. L. Wang and J. Song, *Science*, 2006, 312, 242-246.

3 J. Wang, X. Li, Y. Zi, S. Wang, Z. Li, L. Zheng, F. Yi, S. Li and Z. L. Wang, *Adv. Mater.*, 2015, **27**, 4830-4836.

4 S. Srinivasan, J. Hiller, B. Kabius and O. Auciello, *Appl. Phys. Lett.*, 2007, **90**.

5 Z. Qian, F. Liu, Y. Hui, S. Kar and M. Rinaldi, *Nano Lett.*, 2015, **15**, 4599-4604.

6 D. Dezest, O. Thomas, F. Mathieu, L. Mazenq, C. Soyer, J. Costecalde, D. Remiens, J. F. Deue and L. Nicu, *J. Micromech. Microeng.*, 2015, **25**.

7 S. L. Calvert, Y. Shen, A. B. Sabater, S. Mohammadi and J. F. Rhoads, *J. Micromech. Microeng.*, 2015, **25**.

8 H. Zhang, Y. Yang, T.-C. Hou, Y. Su, C. Hu, Z. L. Wang, *Nano Energy*, 2013, **2**, 1019-1024.

9 Qin, Y.; Wang, X.; Wang, Z. L., *Nature*, 2008, **451**, 809−813.

10 Wu, W.; Bai, S.; Yuan, M.; Qin, Y.; Wang, Z. L.; Jing, T., *ACS Nano*, 2012, **6**, 6231-6235.

11 Bai, S.; Zhang, L.; Xu, Q.; Zheng, Y.; Qin, Y.; Wang, Z. L., *Nano Energy*, 2013, **2**, 749-753.

12 N. Jalali, P. Woolliams, M. Stewart, P. M. Weaver, M. G. Cain, S. Dunn and J. Briscoe, *J. Mater. Chem. A*, 2014, **2**, 10945-10951.

13 R. Yu, C. Pan, J. Chen, G. Zhu and Z. L. Wang, *Adv. Funct. Mater.*, 2013, **23**, 5868-5874.

14 P.-N. Ni, C.-X. Shan, S.-P. Wang, X.-Y. Liu and D.-Z. Shen, *J. Mater. Chem. C*, 2013, **1**, 4445-4449.

15 K. C. Pradel, W. Wu, Y. Zhou, X. Wen, Y. Ding and Z. L. Wang, *Nano Lett.*, 2013, **13**, 2647-2653.

16 Y. Zhang, X. Yan, Y. Yang, Y. Huang, Q. Liao and J. Qi, *Adv. Mater.*, 2012, **24**, 4647-4655.

17 B. P. Nabar, Z. Celik-Butler and D. P. Butler, *Nano Energy*, 2014, **10**, 71-82.

18 B. Kumar and S.-W. Kim, *Nano Energy*, 2012, **1**, 342-355.

19 J. Briscoe and S. Dunn, *Nano Energy*, 2015, **14**, 15-29.

20 G.-T. Hwang, J. Yang, S. H. Yang, H.-Y. Lee, M. Lee, D. Y. Park, J. H. Han, S. J. Lee, C. K. Jeong, J. Kim, K.-I. Park and K. J. Lee, *Adv. Energy. Mater.*, 2015, **5**.

21 X. Chen, S. Xu, N. Yao and Y. Shi, *Nano Lett.*, 2010, **10**, 2133-2137.

22 J. Rödel, W. Jo, K. T. P. Seifert, E.-M. Anton, T. Granzow, and D. Damjanovic, *J. Am. Ceram. Soc.*, 2009, **92,** 1153-1177.

23 D. Maurya, Y. Zhou, Y. Yan, and S. Priya, *J. Mater. Chem. C,* 2013, **1**, 2102-2111.

24 D. Maurya, A. Pramanick, M. Feygenson, J. C. Neuefeind, R. J. Bodnar and S. Priya, *J. Mater. Chem. C*, 2014, **2**, 8423-8431.

25 C. Jiang, K. Zhou, X. Zhou, Z. Li, and D. Zhang, *Ceram. Int.*, 2015, **41**, 6858-6862.

26 C. Jiang, X. Zhou, K. Zhou, C. Chen, H. Luo, X. Yuan and D. Zhang, *J. Eur. Ceram. Soc.*, 2016, **36**, 1377-1383.

27 J. T. Zeng, K. W. Kwok, W. K. Tam, H. Y. Tian, X. P. Jiang, and H. L. W. Chan, *J. Am. Ceram. Soc.*, 2006, **89**, 3850-3853.

28 H. Zhang, P. Xu, E. Patterson, J. Zang, S. Jiang, J. Roedel., *J. Eur. Ceram. Soc.* 2015, **35**, 2501-2512.

29 H. Zhang, C. Groh, Q. Zhang, W. Jo, KG Webber, J. Rödel., *Adv. Electron. Mater.* 2015, **1**, 1500018.

30 J. Li, G. Wang, H. Wang, C. Tang, Y. Wang, C. Liang, W. Cai and L. Zhang, *J. Mater. Chem.*, 2009, **19**, 2253-2258.

31 I. Levin and I. M. Reaney, *Adv. Funct. Mater.*, 2012, **22**, 3445-3452.

32 C. Ma, H. Guo, and X. Tan, *Adv. Funct. Mater.*, 2013, **23**, 5261-5266.

33 C. Ma, H. Guo, S. P. Beckman, and X. Tan, *Phys. Rev. Lett.*, 2012, **109**, 17602.

34 R. Dittmer, W. Jo, J. Rödel, S. Kalinin, and N. Balke, *Adv. Funct. Mater.*, 2012, **22**, 4208-4215.

35 D. Maurya, V. Petkov, A. Kumar and S. Priya, *Dalton Trans.*, 2012, **41**, 5643-5652.

36 C. Jiang, D. Zhang, K. Zhou, X. Zhou, H. Luo, I. Abrahams, *J. Mater. Chem. A*, 2016, **4**, 18050-18059.

37 J. Jiang, Y. Li, J. Liu, X. Huang, C. Yuan and X. W. Lou, *Adv. Mater.*, 2012, **24**, 5166-5180.

38 A. Koka, Z. Zhou, H. Tang and H. A. Sodano, *Nanotechnology*, 2014, **25**.

39 F. Fang, X. Chen, Z. Du, Z. Zhu, X. Chen, H. Wang and P. Wu, *Polymers*, 2015, **7**, 1577-1586.

40 S. Bukkapatnam, S. Kamarthi, Q. Huang, A. Zeid and R. Komanduri, *IEEE Trans.*, 2012, **44**, 492-495.

41 X. Jiang, W. Huang and S. Zhang, *Nano Energy*, 2013, **2**, 1079-1092.

42 A. C. Larson, R. B. Von Dreele, *Los Alamos National Laboratory Report*, No. LAUR-86-748, (1987).

43 P.E.R. Blanchard, S. Liu, B.J. Kennedy, C.D. Ling, Z. Zhang, M. Avdeev, L.Y. Jang, J.F. Lee, C.W. Pao, J.L. Chen, *Dalton Trans*., 2014, **43**, 17358-17365.

44 G. O. Jones and P. A. Thomas, *Acta Crystallogr*., 2002, **B58**, 168-178.

45 R. D. Shannon, *Acta Crystallogr*., 1976, **A32**, 751-767.

46 W. Zhao, H. Zhou, Y. Yan and D. Liu, *J. Am. Ceram. Soc.*, 2008, **91**, 1322-1325.

47 H. Simons, J. Daniels, W. Jo, R. Dittmer, A. Studer, M. Avdeev, J. Rödel, and M. Hoffman, *Appl. Phys. Lett*., 2011, **98**, 082901.

48 Jaffe B, Cook WR, Jaffe H. Piezoelectric ceramics. *London: Academic Press;* 1971. p. 53–114.

49 G. Arlt, *J. Mater. Sci.*, **25**, 2655-2666.

50 P. Zheng, J. L. Zhang, Y. Q. Tan and C. L. Wang, *Acta Mater.*, 2012, **60**, 5022-5030.

Table 1 Refinement details and refined structural parameters for NBBT platelets before and after polarization.

	Before poling	**After poling**
Chemical formula	$Na_{0.465}Bi_{0.465}Ba_{0.07}TiO_3$	$Na_{0.465}Bi_{0.465}Ba_{0.07}TiO_3$
Formula weight	213.37 g mol^{-1}	213.37 g mol^{-1}
Sample description	Pale yellow platelets	Pale yellow platelets
Phase 1		
Crystal system	Tetragonal	Tetragonal
Space group	*P4bm*	*P4bm*
Unit cell dimensions	*a* = 5.4826(2) Å	*a* = 5.4995(2) Å
	c = 3.88462(8) Å	*c* = 3.90046(9) Å
Volume	116.770 (6) $Å^3$	117.968 (9) $Å^3$
Z	2	2
Density (calculated)	6.069 Mg m^{-3}	6.007 Mg m^{-3}
Weight fraction	0.555(3)	0.495(5)
Texture index	2.947	3.049
Phase 2		
Crystal system	Monoclinic	Monoclinic
Space group	*Cc*	*Cc*
Unit cell dimensions	*a* = 9.5354(3) Å	*a* = 9.5502(4) Å
	b = 5.5200(4) Å	*b* = 5.5360(2) Å
	c = 5.5942(5) Å	*c* = 5.6206(3) Å
	β = 125.472(2)°	β = 125.401(1)°
Volume	239.80(2) $Å^3$	242.22(1) $Å^3$
Z	4	4
Density (calculated)	5.910 Mg m^{-3}	5.851 Mg m^{-3}
Weight fraction	0.445(13)	0.505(10)
Texture index[a]	3.575	3.119
R-factors[a]	R_{wp} = 0.0678	R_{wp} = 0.0760
	R_p = 0.0530	R_p = 0.0566
	R_{ex} = 0.0234	R_{ex} = 0.0297
	R_F2 = 0.1149	R_F2 = 0.1572
	χ^2 = 8.466	χ^2 = 6.597
No. of variables	75	75
No of profile points used	8122	8122
No of reflections	350	350

[a]For definition of R-factors and texture index see reference 42

Figure captions

Fig.1. Detail of the X-ray diffraction pattern of NBBT before (lower) and after (upper) poling corresponding to the (110) peak of the pseudo-cubic perovskite subcell. Reflections due to the *Cc* (asterisks) and *P*4*bm* (triangles) are indicated.

Fig. 2 Fitted X-ray diffraction profiles for NBBT platelets (a) as prepared and (b) after poling showing observed (points) calculated (line) and difference (lower) profiles. Reflection positions are indicated by markers: tetragonal phase (lower) and monoclinic phase (upper). Detail of the fits are inset.

Fig. 3 Scanning electron microscopy images of (a) the NBIT platelets synthesized by the molten-salt synthesis process, and (b) the NBBT templates by a topochemical reaction method.

Fig. 4 Na, Bi, Ba, Ti and O SEM EDX mapping images of an NBBT platelet.

Fig. 5 HRTEM images viewed down the [010] zone axis of (a) an NBIT platelet; (b) a platelet showing both NBIT and NBBT structures, with a transitional area showing features of both structures indicated by red lines and (c) an NBBT platelet. Insets in (a) and (c) show fast Fourier transforms of selected areas. Characteristic *d*-spacings are shown.

Fig. 6 (a) Detail of the high resolution TEM image of a partially converted NBIT platelet, with bismuthate and perovskite blocks of NBIT indicated (above) as well as the perovskite structure of NBBT (below); (b) schematic illustration of the topochemical conversion from layer-structured NBIT to perovskite NBBT.

Fig. 7 Bright field TEM images {(a) and (c)} and selected area diffraction patterns along the [001] zone axis {(b) and (d)} of a platelet of as prepared NBBT {(a) and (b)} and a platelet poled at 8 kV/mm {(c) and (d)}.

Fig. 8 PFM images of ferroelectric domains for an unpoled NBBT platelet: (a) to (c) and an NBBT platelet poled at 8 kV/mm, where (a) and (d) correspond to height (b) and (e) to amplitude and (c) and (f) to phase images.

Fig. 9 PFM characterization of NBBT platelets, (a) phase-voltage hysteresis; (b) amplitude-voltage butterfly loops.

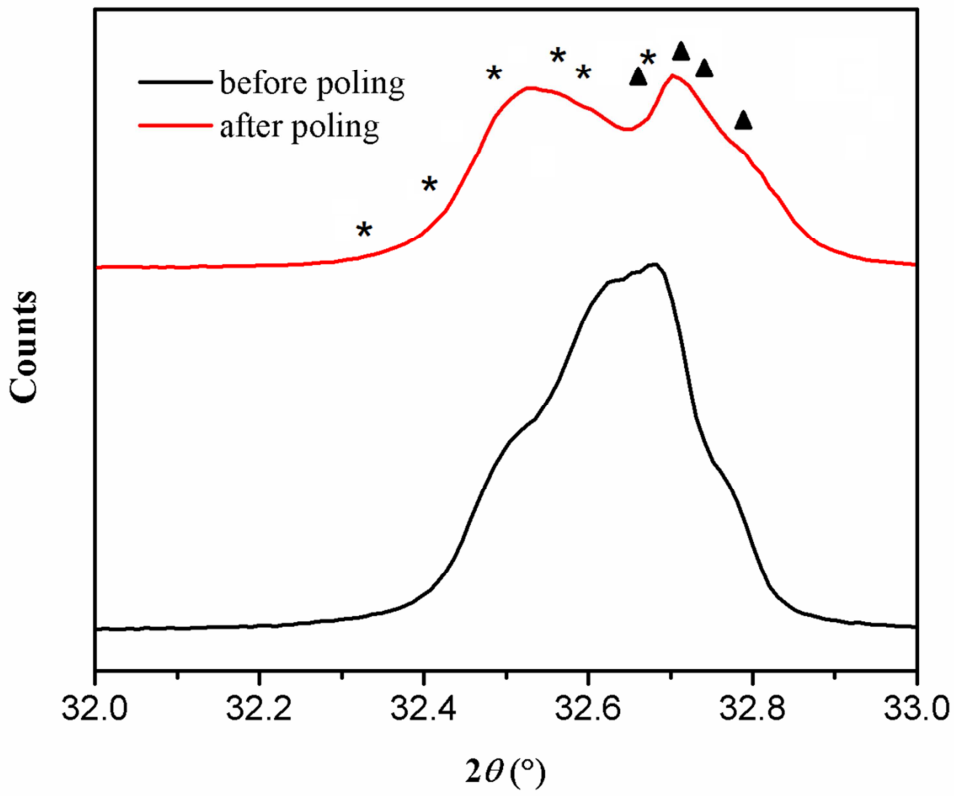

Fig.1

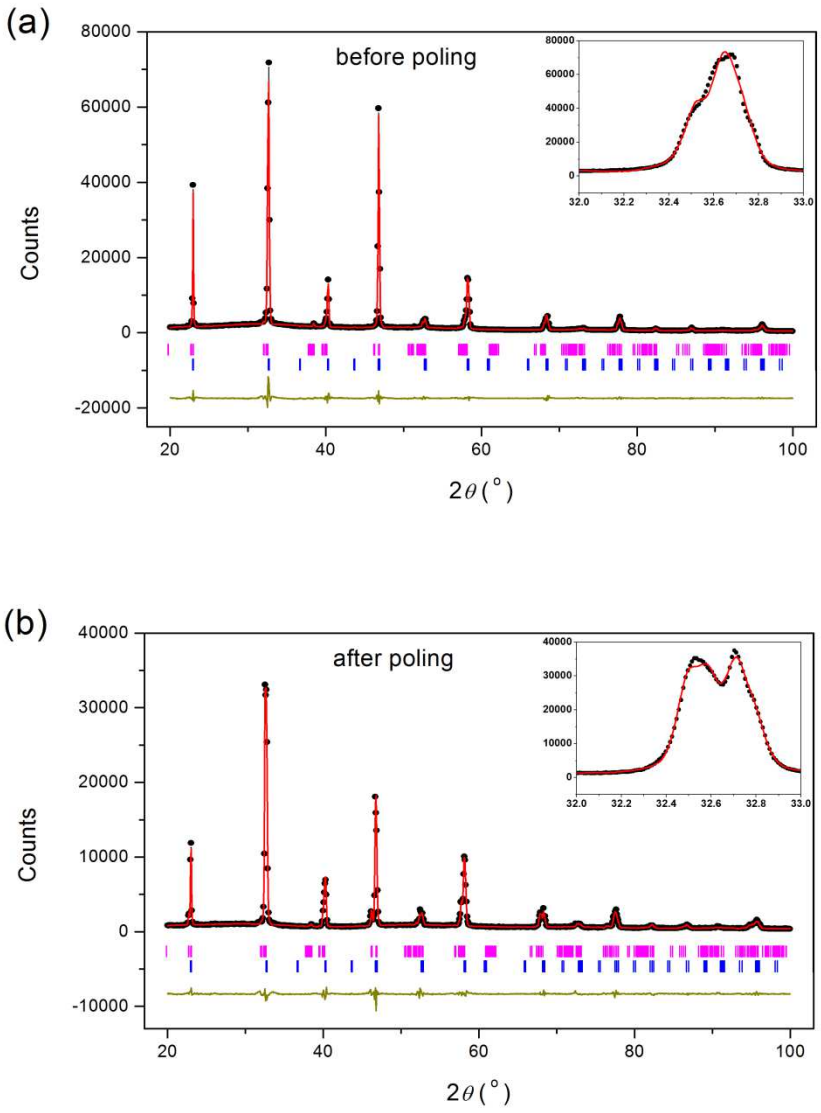

Fig.2

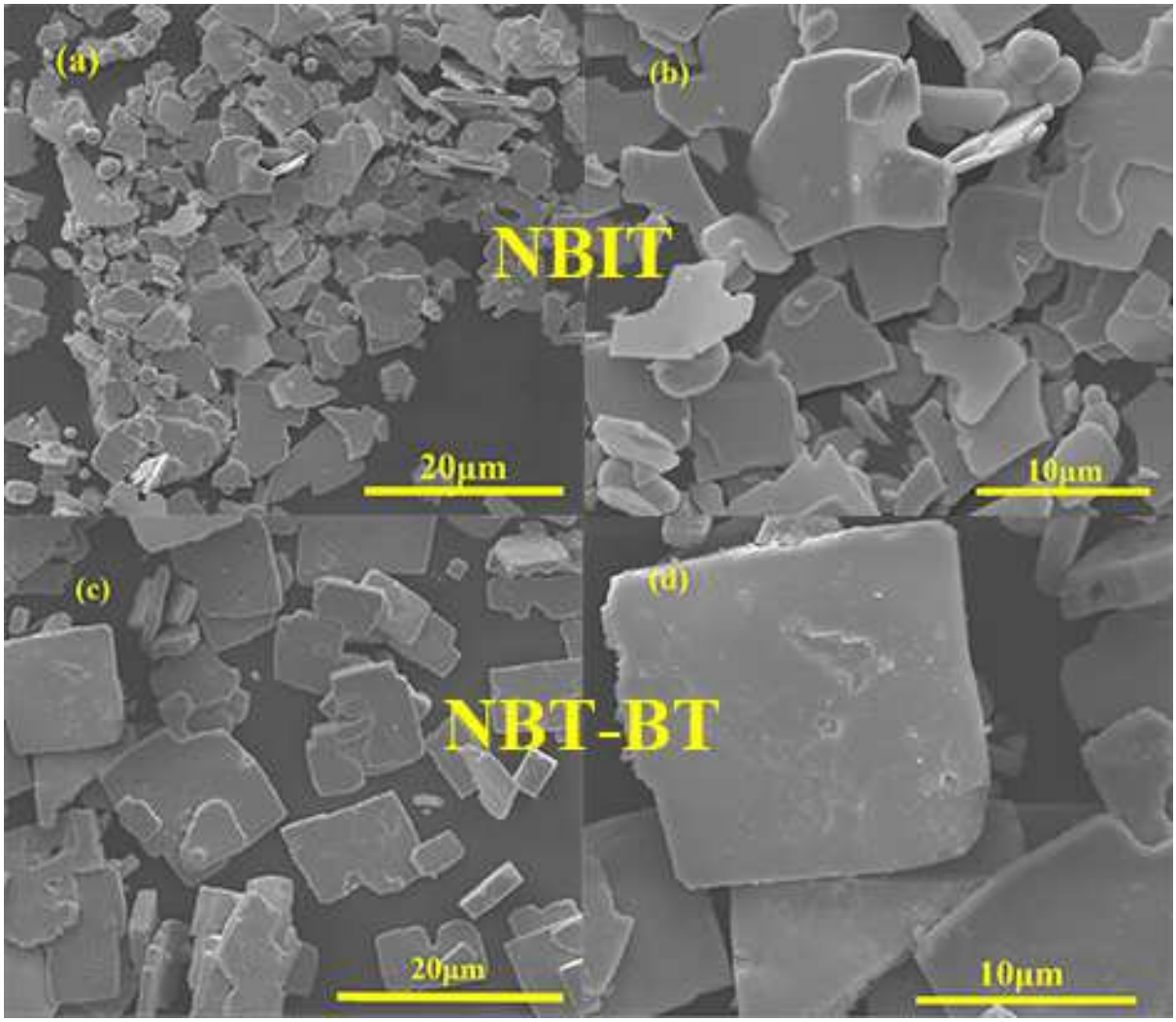

Fig. 3

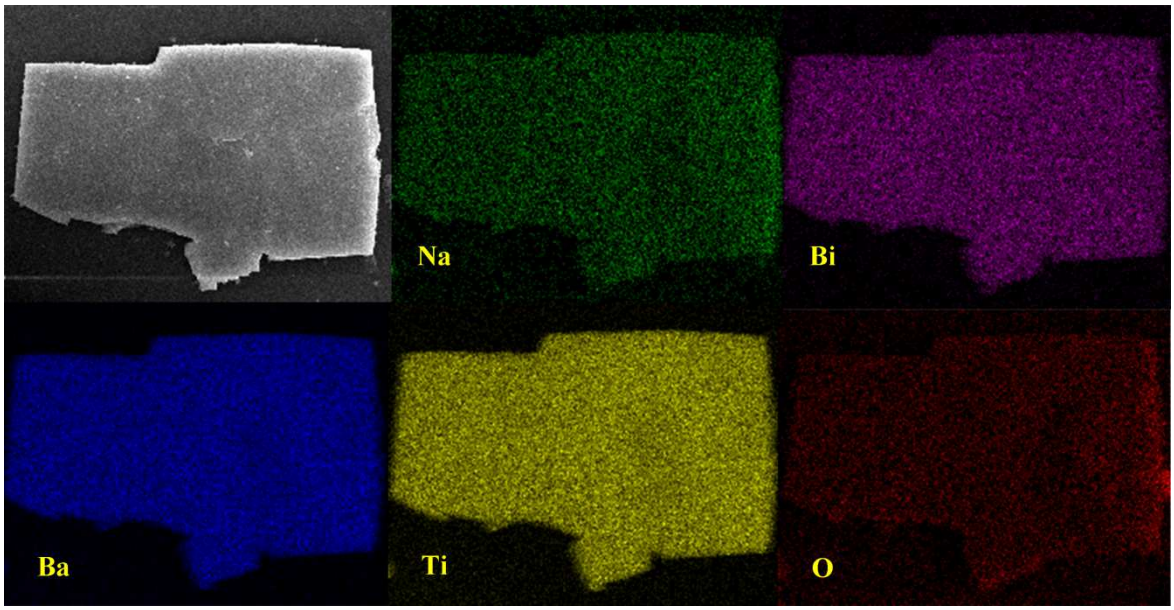

Fig. 4

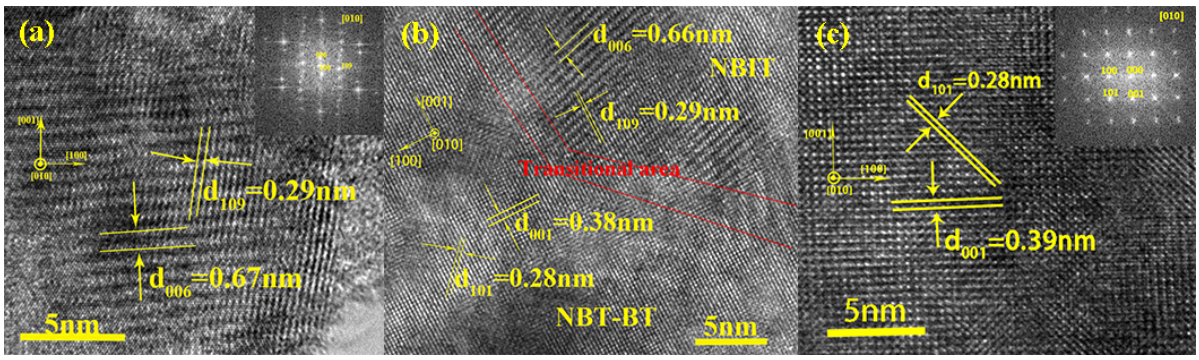
(a)
d_{109}=0.29nm
d_{006}=0.67nm
5nm
(b)
d_{006}=0.66nm
NBT
d_{109}=0.29nm
Transitional area
d_{001}=0.38nm
d_{101}=0.28nm
NBT-BT
5nm
(c)
d_{101}=0.28nm
d_{001}=0.39nm
5nm

Fig.5

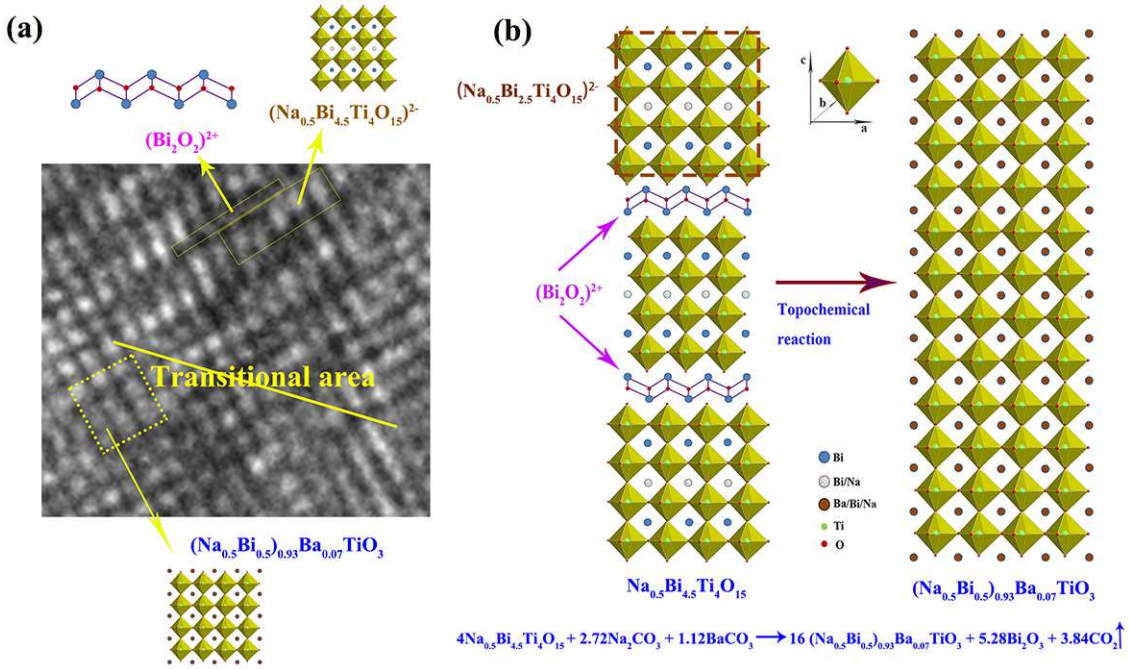
(a)
$(Na_{0.5}Bi_{4.5}Ti_4O_{15})^{2-}$
$(Bi_2O_2)^{2+}$
Transitional area
$(Na_{0.5}Bi_{0.5})_{0.93}Ba_{0.07}TiO_3$
(b)
$(Na_{0.5}Bi_{2.5}Ti_4O_{15})^{2-}$
$(Bi_2O_2)^{2+}$
Topochemical reaction
Bi
Bi/Na
Ba/Bi/Na
Ti
O
$Na_{0.5}Bi_{4.5}Ti_4O_{15}$
$(Na_{0.5}Bi_{0.5})_{0.93}Ba_{0.07}TiO_3$
$4Na_{0.5}Bi_{4.5}Ti_4O_{15} + 2.72Na_2CO_3 + 1.12BaCO_3 \rightarrow 16\,(Na_{0.5}Bi_{0.5})_{0.93}Ba_{0.07}TiO_3 + 5.28Bi_2O_3 + 3.84CO_2\uparrow$

Fig. 6

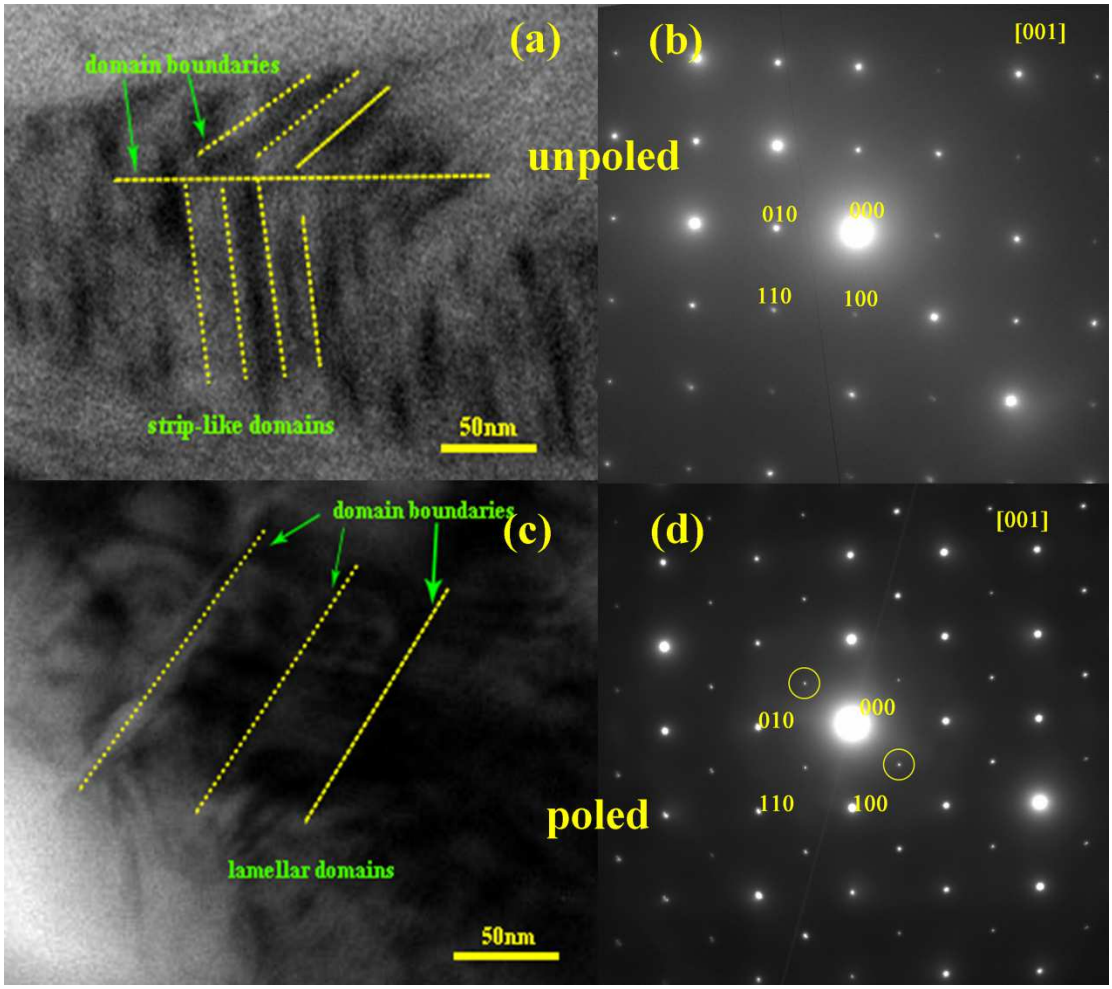
(a)
(b)
[001]
domain boundaries
unpoled
010
000
110
100
strip-like domains
50nm
domain boundaries
(c)
(d)
[001]
010
000
poled
110
100
lamellar domains
50nm

Fig. 7

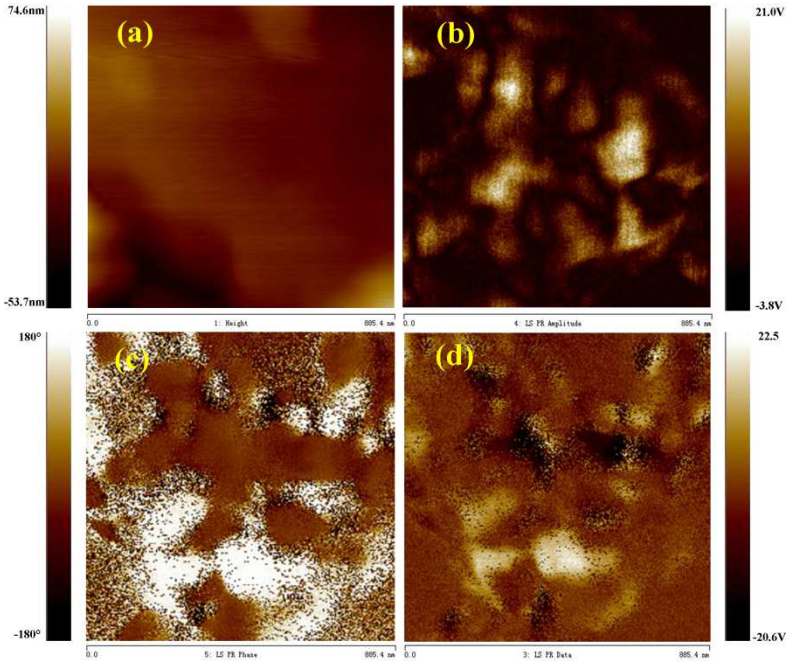
74.6nm
-53.7nm
(a)
(b)
21.0V
-3.8V
180°
-180°
(c)
(d)
22.5
-20.6V

Fig. 8

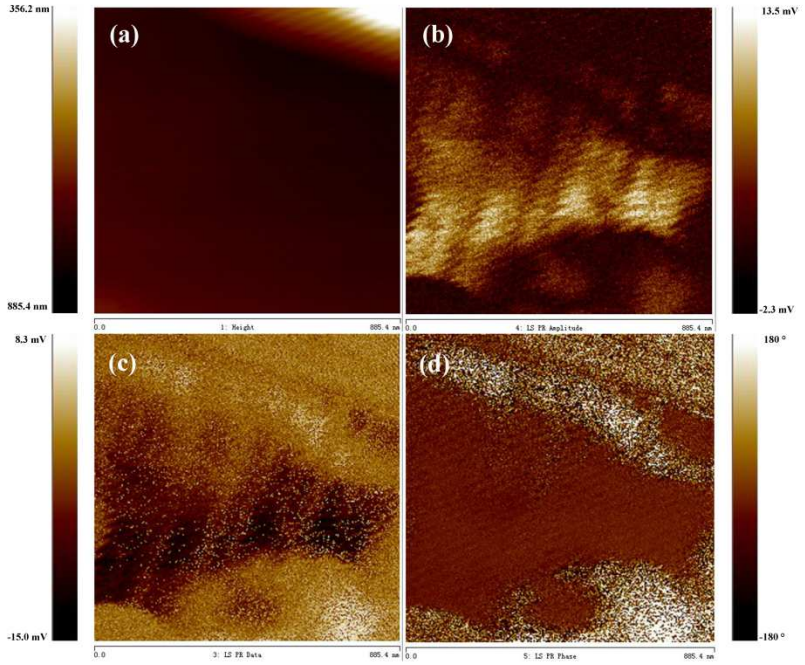
356.2 nm
885.4 nm
(a)
(b)
13.5 mV
-2.3 mV
8.3 mV
-15.0 mV
(c)
(d)
180 °
-180 °

Fig. 9

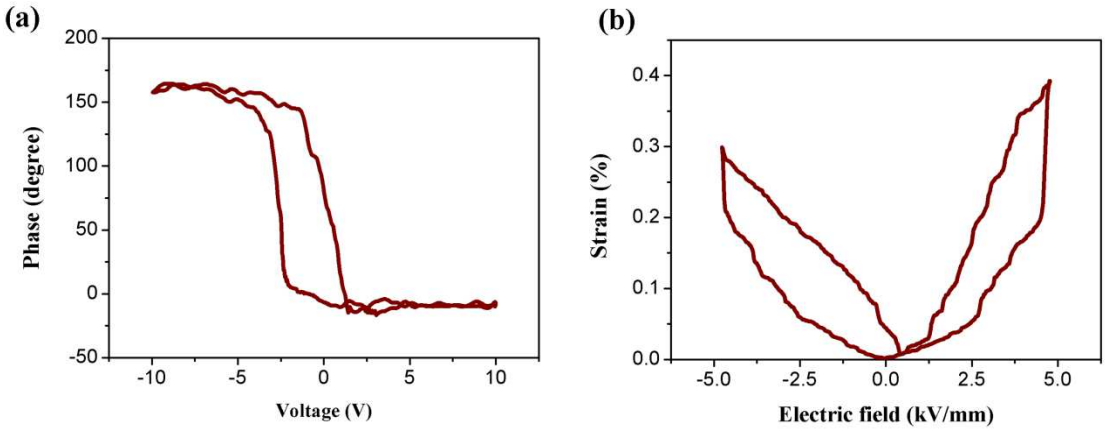
(a)
Phase (degree)
200
150
100
50
0
-50
-10
-5
0
5
10
Voltage (V)
(b)
Strain (%)
0.4
0.3
0.2
0.1
0.0
-5.0
-2.5
0.0
2.5
5.0
Electric field (kV/mm)

Fig. 10